



# Vision-based control of robotic manipulator for citrus harvesting<sup>☆</sup>

S.S. Mehta<sup>a,\*</sup>, T.F. Burks<sup>b</sup>

<sup>a</sup> Department of Industrial and Systems Engineering, Research and Engineering Education Facility, University of Florida, Shalimar, FL 32579, United States

<sup>b</sup> Department of Agricultural and Biological Engineering, University of Florida, Gainesville, FL 32611, United States



## ARTICLE INFO

### Article history:

Received 30 August 2013

Received in revised form 29 December 2013

Accepted 6 January 2014

### Keywords:

Visual servo control

Robotic harvesting

Agricultural robotics

## ABSTRACT

The main contribution of this paper is in the development of vision-based estimation and control system for robotic fruit harvesting and rigorous stability analysis to guarantee performance of the closed-loop system. The presented cooperative visual servo controller benefits from the large field-of-view of a fixed camera and the accuracy of a camera-in-hand (CiH). Computationally inexpensive perspective transformation-based range estimation method obtains 3D fruit position using a monocular camera to enable real-time manipulator control. A rotation controller is developed to orient the robot such that the target fruit selected by the fixed camera can be viewed by the CiH attached to the end-effector. Subsequently, the end-effector can be servoed to the target fruit location using the presented pursuit guidance based hybrid translation controller. Lyapunov-based stability analysis guarantees global exponential regulation of the end-effector. Numerical simulations verify the feasibility of the developed controller while the performance is evaluated on a seven degrees-of-freedom kinematically redundant manipulator using an artificial citrus tree. The position of the fruit was randomly selected, and the closed-loop visual servo control experiment was performed 21 times to analyze the repeatability and accuracy of the developed controller. With 95% confidence level the expected position of the robot end-effector is observed to lie within the confidence ellipsoid. The accuracy of the controller was observed to be about 15 mm, thus making the system suitable for harvesting medium and large varieties of citrus fruit but may limit operation for small varieties such as page and blood oranges.

© 2014 Elsevier B.V. All rights reserved.

## 1. Introduction

The United States (US) citrus industry is facing growing global market pressures that threaten its long-term viability. For instance, Brazilian orange growers can produce, harvest, process, and ship juice to US (Muraro et al., 2000), and European (Spreen and Muraro, 2000) markets at less cost than can Florida growers. The combination of low commodity prices both domestically and abroad, high US labor prices, and low labor productivity present significant challenges for US citrus. Florida citrus, approximately 580,000 acres, has harvesting costs currently exceeding their cost of production, and approaches four times Brazilian harvesting cost. According to economic studies, harvesting costs must be reduced

<sup>☆</sup> This research is supported in part by a grant from the United States Department of Agriculture Small Business Innovation Research (USDA-SBIR) award contract #2012-00032, the AFRL Mathematical Modeling and Optimization Institute contract #FA8651-08-D-0108/042, and the USDA NIFA AFRI National Robotics Initiative #2013-67021-21074. Any opinions, findings and conclusions or recommendations expressed in this material are those of the author(s) and do not necessarily reflect the views of the funding agency.

\* Corresponding author. Tel.: +1 (850) 833 9350; fax: +1 (850) 833 9366.

E-mail addresses: [siddhart@ufl.edu](mailto:siddhart@ufl.edu) (S.S. Mehta), [tburks@ufl.edu](mailto:tburks@ufl.edu) (T.F. Burks).

by 50% to maintain global competitiveness (Brown, 2002). In this respect, mechanization of fruit harvesting is highly desirable in the US as well as other developed nations. Typical mechanized fruit harvesting technology, such as trunk shaker and canopy shaker, have limitations for soft fruit harvesting because of the occurrence of excessive damage to the harvest. Fruit damage is typical to these mass harvesting systems since they are based on the principle of shaking or knocking the fruit out of the tree. An alternative to mechanized fruit harvesting systems is the use of autonomous robotic system, which could potentially yield superior fruit quality.

The first major program in robotic fruit harvesting worldwide was begun at the University of Florida in 1980s by Harrell et al. (1990b). Subsequently, numerous researchers around the world studied robotic solutions for fresh market fruit as well as vegetable harvesting. A comprehensive review of robotic systems in agriculture can be found in Tillett (1993); Sarig (1993); Hannan and Burks (2004); Li et al. (2011). Ceres et al. (1998) developed an-aided fruit harvesting strategy, where an operator performed detection of fruits by means of a laser rangefinder (LRF). The identified position of the fruit in spherical coordinates was used to control the three degrees-of-freedom (DOF) manipulator for harvesting. d'Esnou (1985); d'Esnou et al. (1987) developed a vision-based three DOF,

hydraulically powered spherical coordinate manipulator – MAGALI – for golden apple harvesting, where a monocular camera detected a fruit during vertical scan. Subsequently, the telescopic arm translated along the optical beam until it reached the fruit, which was sensed by a photoelectric sensor. Ceres et al. (1998); d'Esnou et al. (1987) relied on open-loop position control, i.e., dead-reckoning, of the manipulator, which may result in inaccuracies due to fruit motion or measurement errors. Florida Citrus Picking Robot in Harrell et al. (1989, 1990a,b) aimed at overcoming the limitations of MAGALI by using a closed-loop camera-in-hand (CiH) configuration along with an ultrasound transducer for fruit range identification. The control gains increased by two orders of magnitude as the robot approached a fruit, raising concern for stability of the system. Compensation was offered by scheduling the gains using range information from the on-board ultrasonic transducer. Levi et al. (1988) investigated a vision-based cylindrical manipulator system for robotic citrus harvesting. Due to chosen camera configuration and dead-reckoning during reaching stage, the harvesting accuracy is susceptible to mechanical backlash, bearing wear, etc. In Rabatel et al. (1995); Juste and Sevilla (1992), the French and Spanish researchers proposed a robotic citrus harvesting system called EUR-EKA. A Bayesian classifier detected mature fruit from the grayscale images captured by a monocular vision system. For the proposed spherical manipulator, the robot motion trajectory was along the straight line between the camera optical center and the fruit. The inadequate fruit depth information was found to be the cause of majority failures. Muscato et al. (2005) developed a vision-based citrus harvesting robot prototype called CRAM, where differential image size of the fruit was used to identify the distance to fruit, thus, avoiding additional range measurement sensors.

Previous research at large focused on the development of robotic manipulators, end-effectors, and target classification methods. Although harvest efficiency, which is the most influential factor in robotic harvesting economics, depends on the stability and performance of the closed-loop control system, relatively little attention has been paid to control formulation and rigorous stability analysis of the harvesting systems. In this paper, a cooperative visual servo controller is developed to regulate a robot end-effector to the target fruit location. Lyapunov-based stability analysis is presented to guarantee uniform global exponential stability of the closed-loop system such that the desired transient performance can be obtained by appropriately selecting the control gains. Similar to Van Henten et al. (2002, 2003), a cooperative vision system consisting of a fixed camera and a CiH is incorporated such that the fixed camera provides a global view of a tree canopy, while the CiH, due to proximity, provides high resolution fruit images. One of the challenges associated with closed-loop harvesting systems is of determining the Euclidean position of a fruit. Apart from using an additional range sensor (Harrell et al., 1989, 1990a,b), the most popular method of determining the Euclidean depth of a fruit is by using stereo-vision or triangulation (Buemi et al., 1996; Kondo et al., 1996; Recce et al., 1996; Van Henten et al., 2002, 2003). However, in contrast to these methods the presented approach uses perspective camera geometry to obtain absolute range estimates. The resulting perspective transformation based range estimation approach is computationally less complex than stereo-vision method thus making it suitable for the real-time harvesting application. A global view from the fixed camera along with the estimated range information can be used to generate a global map of fruit locations from which a target fruit can be selected for harvesting using a pre-determined criteria. A rotation controller is developed to orient the robot end-effector towards the target fruit such that the fruit enters the field-of-view (FOV) of the CiH. This enables harvesting fruits that were not initially visible to the CiH. Subsequently, the developed pursuit guidance based hybrid translation controller regulates the end-effector to the Euclidean fruit location. For improved dexterity

and accuracy, a seven DOF kinematically redundant, electric motor driven manipulator is selected for the task. The performance of the developed controller is verified through numerical simulations and by conducting experiments on an artificial citrus tree with randomly attached fruits.

The presented paper is organized as follows: Section 2 introduces various coordinate frames and provides the perspective transformation-based range estimation method for Euclidean reconstruction; Section 3 states the control objective of regulating the end-effector to the target fruit; rotation controller to orient the end-effector towards the fruit and hybrid translation controller are developed in Section 4; the stability analysis presented in Section 5 proves exponential set-point regulation; Simulation results presented in Section 6 verify the feasibility of the developed controller; Section 7 provides experimental evidence to verify the range estimation method and validate the proposed controller for citrus harvesting; concluding remarks are presented in Section 8. Appendix A discusses various challenges pertaining to real systems and how the developed controller performs in these scenarios.

## 2. Euclidean reconstruction

Consider the orthogonal coordinate frames  $\mathcal{F}$ ,  $\mathcal{F}_f$ , and  $\mathcal{F}_b$  as shown in Fig. 1. The time-varying coordinate frame  $\mathcal{F}$  is attached to a CiH, i.e., a camera held by a robot end-effector. The coordinate frame  $\mathcal{F}_f$  is attached to a fixed camera, for example, a stationary camera mounted in the workspace of a robot, and the coordinate frame  $\mathcal{F}_b$  is attached to the stationary base of a robot.  $O^* \in \mathbb{R}^3$  denotes the fruit position measured in the base frame  $\mathcal{F}_b$ . The unknown Euclidean coordinates of the fruit center,  $\bar{m}(t), \bar{m}_f \in \mathbb{R}^3$ , expressed in terms of  $\mathcal{F}$  and  $\mathcal{F}_f$ , respectively, are given as

$$\bar{m}(t) = [x(t) \ y(t) \ z(t)]^T, \quad \bar{m}_f = [x_f \ y_f \ z_f]^T \quad (1)$$

where  $z(t), z_f \in \mathbb{R}$  denote the unknown depth of the target fruit expressed in  $\mathcal{F}$  and  $\mathcal{F}_f$ , respectively.

The Euclidean-space is projected onto the image-space, so let  $m_i(t)$  and  $m_f$  denote the corresponding normalized Euclidean coordinates of the fruit center as

$$m(t) = \frac{\bar{m}(t)}{z(t)} = \begin{bmatrix} \frac{x(t)}{z(t)} & \frac{y(t)}{z(t)} & 1 \end{bmatrix}^T, \quad (2)$$

$$m_f = \frac{\bar{m}_f}{z_f} = \begin{bmatrix} \frac{x_f}{z_f} & \frac{y_f}{z_f} & 1 \end{bmatrix}^T.$$

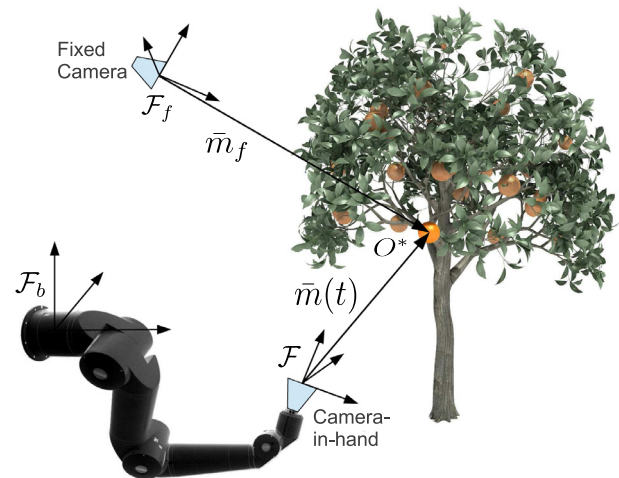


Fig. 1. Coordinate frame relationships, where the time-varying frame  $\mathcal{F}$  is attached to the CiH,  $\mathcal{F}_f$  corresponds to the fixed camera, and  $\mathcal{F}_b$  is attached to the stationary base of the robot.

**Assumption 1.** In (2), it is assumed that the unknown depths  $z(t), z_f > \varepsilon$ , where  $\varepsilon \in \mathbb{R}_{>0}$  is a constant. This is a standard assumption in visual servo control, which physically means that the target is always in front of the camera. In practice,  $\varepsilon$  should be equal to or greater than the minimum focusing distance of a camera lens for the objects to be clearly visible.

In addition to having normalized task-space coordinates, the target point will also have pixel coordinates acquired by the CiH and the fixed camera. Let  $p(t), p_f \in \mathbb{R}^2$  denote the pixel coordinates of the target center expressed in  $\mathcal{F}$  and  $\mathcal{F}_f$ , respectively, as

$$p(t) \triangleq [u(t) \ v(t)]^T, \quad p_f \triangleq [u_f \ v_f]^T. \quad (3)$$

Since the normalized Euclidean coordinates in (2) cannot be measured directly, a global invertible transformation (i.e., the pinhole camera model) is used to determine the normalized Euclidean coordinates from the corresponding pixel information as

$$\begin{bmatrix} p^T & 1 \end{bmatrix}^T = A_m, \quad \begin{bmatrix} p_f^T & 1 \end{bmatrix}^T = A_f m_f. \quad (4)$$

In (4),  $A, A_f \in \mathbb{R}^{3 \times 3}$  denote the known, constant, invertible, intrinsic camera calibration matrices defined as

$$A \triangleq \begin{bmatrix} \lambda_{xf} & -\lambda_{xf} \cot \phi & u_0 \\ 0 & \frac{\lambda_{yf}}{\sin \phi} & v_0 \\ 0 & 0 & 1 \end{bmatrix}, \quad A_f \triangleq \begin{bmatrix} \lambda_{xf} f_f & -\lambda_{xf} f_f \cot \phi_f & u_{of} \\ 0 & \frac{\lambda_{yf} f_f}{\sin \phi_f} & v_{of} \\ 0 & 0 & 1 \end{bmatrix} \quad (5)$$

where  $u_0, v_0 \in \mathbb{R}$  and  $u_{of}, v_{of} \in \mathbb{R}$  denote the pixel coordinates of the principal point (i.e., the intersection of an optical axis with the image plane) of the CiH and the fixed camera, respectively. The constants  $f, f_f \in \mathbb{R}$  represent the focal length of the CiH and the fixed camera, respectively,  $\lambda_x, \lambda_{xf} \in \mathbb{R}$  and  $\lambda_y, \lambda_{yf} \in \mathbb{R}$  are the scaling factors in image  $x$  and  $y$  directions of the CiH and the fixed camera, respectively, and  $\phi, \phi_f \in \mathbb{R}$  are the skew angles between camera axes of the CiH and the fixed camera, respectively. The above defined parameters can be obtained by calibrating the cameras, for example, using the approach in Zhang (2000).

To regulate the robot to a target fruit, the 3D Euclidean position of the target can be obtained from the corresponding image coordinates. A perspective transformation based range estimation method is presented to estimate the depth to a fruit. A general expression for the depth estimate is obtained for any fruit with ellipsoidal geometry (e.g., orange, peach, apple). For a given variety to be harvested, it is assumed that the sample mean major and minor axes of the fruit are known *a priori*. Based on the assumption that the actual fruit size is in the vicinity of the sample mean size, the Euclidean depth of the fruit can be estimated using perspective transformation as<sup>1</sup>

$$\hat{z}_f = \frac{f_f (\lambda_{xf} d_{ox} d_{iy} + \lambda_{yf} d_{oy} d_{ix})}{2 d_{ix} d_{iy}} \quad (6)$$

$$d_{ix} = 2 \left( \frac{A_p}{\pi \sqrt{1 - e^2}} \right)^{1/2} \quad d_{iy} = 2 \left( \frac{A_p \sqrt{1 - e^2}}{\pi} \right)^{1/2} \quad (7)$$

where  $\hat{z}_f \in \mathbb{R}$  denotes the estimated Euclidean depth of a fruit measured in  $\mathcal{F}_f$ ,  $d_{ox}, d_{oy} \in \mathbb{R}$  denote the sample mean major and minor axes, respectively, of a fruit,  $d_{ix}, d_{iy} \in \mathbb{R}$  denote the major and minor axes, respectively, of an ellipse in the image plane,  $A_p \in \mathbb{R}$  denotes the measurable area (in pixels) of the fruit in the image plane of the fixed camera,  $e \in \mathbb{R}$  is the known eccentricity of the ellipse,

and  $f_f, \lambda_{xf}, \lambda_{yf}$  are defined in (5). The presented perspective transformation based range estimation method relies on simple color thresholding-based techniques for fruit detection to obtain  $A_p$ , following which the expressions in (6) and (7) can be used to obtain an estimated depth to a fruit. Therefore, the method has less time complexity than the state-of-the-art depth estimation methods using the popular stereo-vision technique, which require computation of a disparity map in addition to fruit detection and depth estimation. Using (2), (6), and (7), the estimated Euclidean position of the fruit in  $\mathcal{F}_f$ , denoted by  $\hat{m}_f \in \mathbb{R}^3$ , can be obtained as

$$\hat{m}_f = m_f \hat{z}_f = \begin{bmatrix} x_f & y_f & 1 \\ z_f & z_f & z_f \end{bmatrix}^T \frac{f_f (\lambda_{xf} d_{ox} d_{iy} + \lambda_{yf} d_{oy} d_{ix})}{2 d_{ix} d_{iy}}. \quad (8)$$

The estimated position of the target obtained in (8) can be expressed with respect to the robot base frame  $\mathcal{F}_b$  through the known extrinsic camera calibration matrix  $A_{ef} \in \mathbb{R}^{4 \times 4}$  as

$$\begin{bmatrix} \hat{m}_b^T & 1 \end{bmatrix}^T = \underbrace{\begin{bmatrix} R_{ef} & t_{ef} \\ \mathbf{0} & 1 \end{bmatrix}}_{A_{ef}} \begin{bmatrix} \hat{m}_f^T & 1 \end{bmatrix}^T \quad (9)$$

where  $R_{ef} \in \mathbb{R}^{3 \times 3}$  and  $t_{ef} \in \mathbb{R}^3$  denote the known rotation and translation of frame  $\mathcal{F}_f$  with respect to  $\mathcal{F}_b$ .

**Remark 1.** When fruit is visible to the CiH, expressions similar to (6)–(8) can be obtained to determine the time-varying depth  $\hat{z}(t)$  and position  $\hat{m}(t) \in \mathbb{R}^3$  of the fruit with respect to  $\mathcal{F}$ . It can easily be shown that since  $d_{ix}/d_{iy}$  is constant, the unknown depth ratio  $\hat{z}/z$  denoted by  $\gamma \in \mathbb{R}_{>0}$  is also constant.

### 3. Control objective

The objective is to locate the robot end-effector to the target fruit position for harvesting, i.e., to regulate the CiH coordinate frame  $\mathcal{F}$  to the target fruit in the sense that  $O_{\mathcal{F}}(t) \rightarrow O^*$ , where  $O_{\mathcal{F}}(t) \in \mathbb{R}^3$  denotes the time-varying position of the frame  $\mathcal{F}$  measured in  $\mathcal{F}_b$ . The control objective can be achieved by regulating the time-varying fruit pixel coordinates  $p(t)$  to the desired image coordinates, and regulating the end-effector to the desired fruit depth. Hence, mathematically, the control objective can be stated as

$$p(t) \rightarrow p_d, p_d = [u_0 \ v_0]^T \text{ and } z(t) \leq z_d \quad (10)$$

where  $z_d \in \mathbb{R}_{>0}$  denotes the maximum desired depth of the fruit in  $\mathcal{F}$ , and  $u_0, v_0 \in \mathbb{R}$  denote the pixel coordinates of the principal point of the CiH.

To control the position and orientation of  $\mathcal{F}$ , a relationship is required to relate the linear and angular camera velocities to the linear and angular velocities of the robot (i.e., the actual kinematic control inputs) that enables the CiH motion. This relationship is dependent on the extrinsic calibration parameters as Malis and Chaumette (2002)

$$\begin{bmatrix} v_c \\ \omega_c \end{bmatrix} = \begin{bmatrix} R_e & [t_e]_{\times} R_e \\ \mathbf{0} & R_e \end{bmatrix} \begin{bmatrix} v_r \\ \omega_r \end{bmatrix} \quad (11)$$

where  $v_c(t), \omega_c(t) \in \mathbb{R}^3$  denote the linear and angular velocity of the CiH,  $v_r(t), \omega_r(t) \in \mathbb{R}^3$  denote the linear and angular velocity of the robot,  $R_e \in \mathbb{R}^{3 \times 3}$  denotes the constant rotation between the CiH and robot end-effector frames, and  $[t_e]_{\times} \in \mathbb{R}^{3 \times 3}$  is a skew symmetric form of  $t_e \in \mathbb{R}^3$ , which denotes the constant translation vector between the CiH and robot frames.

<sup>1</sup> The depth estimator in (6) assumes complete visibility of the fruit. In the presence of partial occlusions or clustered fruit, advanced methods such as perimeter detection and shape analysis techniques Hannan et al. (2009) can be used to obtain the image-space diameters  $d_{ix}, d_{iy}$  of the fruit to get  $\hat{z}_f$  (see Appendix A).

#### 4. Control development

Based on the control objective in Section 3, a decoupled rotation and hybrid translation controller is developed in this section. The fixed camera can view the entire tree canopy and select the fruit to be harvested. However, the target fruit selected by the fixed camera may not be visible to the CiH; therefore, the CiH needs to be oriented along the target fruit. Following the orientation, the CiH can be regulated to the fruit position using the developed translation controller.

##### 4.1. Rotation controller

In this section, a controller is developed to orient the robot end-effector such that the target fruit is in the FOV of the CiH. The estimated fruit position  $\hat{m}_b$  in (9) can be expressed in frame  $\mathcal{F}$  as

$$[\hat{m}^T(t) \ 1]^T = \zeta_r^{-1} [\hat{m}_b^T \ 1]^T = \begin{bmatrix} R_r & t_r \\ \mathbf{0} & 1 \end{bmatrix}^{-1} [\hat{m}_b^T \ 1]^T \quad (12)$$

where  $\zeta_r(t) \in \mathbb{SE}(3)$  includes the position  $t_r(t) \in \mathbb{R}^3$  and orientation  $R_r(t) \in \mathbb{R}^{3 \times 3}$  of the CiH coordinate frame  $\mathcal{F}$  with respect to  $\mathcal{F}_b$ . The transformation matrix  $\zeta_r(t)$  can be obtained from the forward kinematic analysis knowing the robot geometry and joint positions.

The rotation error  $e_\omega(t) \in \mathbb{R}^3$  defined as orientation mismatch to bring the target fruit in the FOV of the CiH can be represented in terms of angle-axis representation as

$$e_\omega \triangleq u\theta \quad (13)$$

where  $u(t) \in \mathbb{R}^3$  represents a unit axis of rotation such that  $u(t) = \frac{\vec{m}'(t)}{\|\vec{m}'(t)\|} \wedge [0 \ 0 \ 1]^T$ , and  $\theta(t) = \cos^{-1}(\frac{\vec{m}'(t)}{\|\vec{m}'(t)\|} \cdot [0 \ 0 \ 1]^T) \in \mathbb{R}$  denotes the rotation angle about  $u(t)$  such that  $0 \leq \theta(t) \leq \pi$ .  $\vec{m}'(t) \in \mathbb{R}^3$  represents a unit vector along  $\hat{m}'$ .

Based on the rotation error in (13), the angular velocity  $\omega_c(t) \in \mathbb{R}^3$  of the CiH can be designed using the following PD controller:

$$\omega_c = -k_{p\omega}e_\omega - k_{d\omega}\dot{e}_\omega \quad (14)$$

where  $k_{p\omega}, k_{d\omega} \in \mathbb{R}_{>0}$  are the proportional and derivative control gains,<sup>2</sup> respectively. Various loop tuning methods, such as Ziegler–Nichols and manual (trial-and-error), can be adopted to determine the control gains. In general, derivative action is susceptible to measurement noise due to numerical differentiation of the input error. However, the above limitation is removed by expressing the unmeasurable time derivative  $\dot{e}_\omega(t) \in \mathbb{R}^3$  as

$$\dot{e}_\omega = L_\omega \omega_c \quad (15)$$

where  $L_\omega(t) \in \mathbb{R}^{3 \times 3}$  is the measurable Jacobian-like function defined as

$$L_\omega = I_3 - \frac{\theta}{2}[u]_\times + \left(1 - \frac{\text{sinc}(\theta)}{\text{sinc}^2(\frac{\theta}{2})}\right)[u]_\times^2. \quad (16)$$

In (16), the  $\text{sinc}(\theta)$  term denotes the unnormalized sinc function, and  $[u]_\times$  is the skew-symmetric matrix of  $u(t)$ . The determinant of  $L_\omega(t)$  is  $\det(L_\omega) = 1/\text{sinc}^2(\theta/2)$ , thus being singular only at  $\theta = 2k\pi \ \forall k \in \mathbb{N}_{>0}$ , i.e., outside of  $0 \leq \theta(t) \leq \pi$ . Using (11), (14), and (15), the angular velocity of the robot end-effector can be obtained as

$$\omega_r = -k_{p\omega}R_e^T(I_3 + k_{d\omega}L_\omega)^{-1}e_\omega \quad (17)$$

where  $I_3$  denotes a  $3 \times 3$  identity matrix.

<sup>2</sup> The proportional gain determines how fast the system output changes for a given change in the input error. A small gain may result in a less sensitive system while too high gain may cause system instability. The derivative gain improves settling time and stability of the system.

##### 4.2. Translation controller

The objective of the translation controller is to regulate the CiH to the target fruit position. Based on the pursuit guidance framework, a hybrid controller is developed to regulate the line-of-bearing to the target fruit to zero. In other words, the centroid of the fruit is regulated to constant image coordinates while approaching the fruit. The hybrid controller uses the image-space fruit position along with the estimated fruit depth in control formulation. Based on the control objective, the translation errors  $e_{v1}(t) \in \mathbb{R}^2$  and  $e_{v2}(t) \in \mathbb{R}$  can be defined as

$$e_{v1} \triangleq p_d - p \quad (18)$$

$$e_{v2} \triangleq z_d - \alpha \hat{z} \quad (19)$$

where  $\hat{z}(t) = [0 \ 0 \ 1]\hat{m}(t)$  is the estimated depth of the target fruit from the CiH, and  $\hat{m}(t)$  is the estimated fruit position in the CiH coordinate frame as stated in Remark 1. The estimated fruit depth  $\hat{z}(t)$  is assumed to be a continuous function of time. In (19),  $\alpha \in \mathbb{R}_{>0}$  denotes a scaling factor such that  $z \leq \alpha \hat{z} \ \forall t$ . The constant  $\alpha$  is selected based on an upper bound on the Euclidean depth estimation error, and, as a rule of thumb,  $\alpha$  can be selected arbitrarily high to ensure that the robot reaches the target fruit despite any estimation errors. Moreover, it will be shown in Appendix A that large values of  $\alpha$  lead to robustness to depth estimation errors. Since  $z \leq \alpha \hat{z}$ , the robot may overshoot the target fruit, and hence the end-effector is equipped with an infrared proximity sensor to stop once the fruit is reached. Let  $v_c(t) \triangleq [v_{cx}(t) \ v_{cy}(t) \ v_{cz}(t)]^T$  be the linear velocity of the CiH and define  $v_{c1} \triangleq [v_{cx}(t) \ v_{cy}(t)]^T$ . Using (19), the linear velocity  $v_{cz}(t)$  along the optical axis of the camera can be obtained using the PD controller as

$$v_{cz} = -k_{pv2}e_{v2} - k_{dv2}\dot{e}_{v2} \quad (20)$$

where  $k_{pv2}, k_{dv2} \in \mathbb{R}_{>0}$  are the proportional and derivative control gains, respectively. Taking the time derivative of (19), the open-loop error system can be obtained as  $\dot{e}_{v2} = \alpha v_{cz}$ . Substituting  $\dot{e}_{v2}$  in (20),  $v_{cz}(t)$  can be obtained in terms of measurable right hand side as

$$v_{cz} = -k_{pv2}(1 + \alpha k_{dv2})^{-1}e_{v2}. \quad (21)$$

Taking the time derivative of the first expression in (4), the velocity of the CiH can be related to the velocity  $\dot{p}(t) \in \mathbb{R}^2$  of the target centroid in the image frame as

$$\dot{p} = \begin{bmatrix} \dot{u} \\ \dot{v} \end{bmatrix} = -\frac{1}{z}J_v v_c - J_\omega \omega_c. \quad (22)$$

In (22),  $J_v(u, v), J_\omega(u, v) \in \mathbb{R}^{2 \times 3}$  are measurable image Jacobians that relate the linear and angular velocity, respectively, of the CiH to the fruit image velocity. Since no orientation change is required during translation control, the image dynamics for translation control can be obtained by substituting  $\omega_c(t) = 0$  in (22) as

$$\dot{p} = -\frac{1}{z}J'_v v_{c1} + \frac{1}{z}J''_v v_{cz} \quad (23)$$

where  $v_{cz}(t) \in \mathbb{R}$  is the control velocity along the optical axis of the camera as obtained in (21),  $J'_v \in \mathbb{R}^{2 \times 2}$  and  $J''_v(u, v) \in \mathbb{R}^2$  are the measurable Jacobians defined as

$$J'_v = \begin{bmatrix} \lambda_x f & 0 \\ 0 & \lambda_y f \end{bmatrix} \quad J''_v = \begin{bmatrix} u \\ v \end{bmatrix}. \quad (24)$$

Using (19), the velocity  $v_{c1} \in \mathbb{R}^2$  along the  $x$  and  $y$ -axis of the CiH can be designed as

$$v_{c1} = -k_{pv1}e_{v1} + k_{dv1}\alpha \dot{p} \quad (25)$$



where  $k_{pv1}, k_{dv1} \in \mathbb{R}_{>0}$  are the proportional and derivative control gains, respectively, such that  $k_{pv1} = k_{pv11} + k_{pv12}$ . The proportional gain  $k_{pv1}$  is selected based on the gain condition established in (47). Substituting (23) in (25), and using the facts  $\dot{z}/z = \gamma$  and  $z \leq \alpha \dot{z}$ , the linear velocity  $v_{c1}(t)$  can be obtained as

$$v_{c1} = -k_{pv1}e_{v1} - \frac{k'_{dv1}}{z}J'_v v_{c1} + \frac{k'_{dv1}}{z}J''_v v_{cz} \quad (26)$$

where  $k'_{dv1} \in \mathbb{R}_{>0}$  is the new derivative control gain. The expression in (26) can be simplified to obtain the linear velocity  $v_{c1}(t)$  in terms of measurable right hand side as

$$v_{c1} = \left( I_2 + \frac{k'_{dv1}}{z}J'_v \right)^{-1} \left( -k_{pv1}e_{v1} + \frac{k'_{dv1}}{z}J''_v v_{cz} \right). \quad (27)$$

From (11), (17), (21), and (27), the linear velocity of robot end-effector can be obtained as

$$v_r = R_e^T (v_c - [t_e]_x R_e \omega_r). \quad (28)$$

## 5. Stability analysis

### 5.1. Rotation controller

**Theorem 1.** The angular velocity control input in (17) ensures global exponential regulation of robot end-effector such that the target fruit is in the FOV of the CiH in the sense that

$$\|e_\omega(t)\| = \zeta_0 \exp\{-\zeta_1 t\} \quad (29)$$

where  $\zeta_0, \zeta_1 \in \mathbb{R}$  denote positive bounding constants.

**Proof.** Let  $V_1(t)$  be defined as the following positive definite Lyapunov function:

$$V_1 = \frac{1}{2} e_\omega^T e_\omega \quad (30)$$

$$\lambda_1 \|e_\omega(t)\|^2 \leq V_1(t) \leq \lambda_2 \|e_\omega(t)\|^2 \quad (31)$$

where  $\lambda_1, \lambda_2 \in \mathbb{R}$  are known positive bounding constants. Taking the time derivative of (30) and substituting the open-loop error dynamics (15) along with the camera angular velocity  $\omega_c(t)$  from (14), we get

$$\dot{V}_1 = -e_\omega^T L_\omega (k_{p\omega} e_\omega + k_{d\omega} \dot{e}_\omega). \quad (32)$$

Using the fact that  $e_\omega^T L_\omega = e_\omega^T$  in (32) and based on the bounding argument in (31), the Lyapunov derivative can be upper bounded as

$$\dot{V}_1 \leq \frac{-k_{p\omega}}{\lambda_2(1+k_{d\omega})} V_1. \quad (33)$$

Consequently, the inequality in (33) can be solved as  $V_1(t) \leq V_1(0) \exp\left\{\frac{-k_{p\omega}}{\lambda_2(1+k_{d\omega})} t\right\}$ , and hence  $e_\omega(t), \dot{e}_\omega(t) \in \mathcal{L}_\infty$  and  $e_\omega(t) \in \mathcal{L}_2$ . Using (13) and (16), and from the fact that  $0 \leq \theta(t) \leq \pi$  and  $e_\omega(t) \in \mathcal{L}_\infty$ , the unit axis  $u(t) \in \mathcal{L}_\infty$  and  $L_\omega \in \mathcal{L}_\infty$ . Using the above arguments, the angular velocity  $\omega_c(t), \omega_r(t) \in \mathcal{L}_\infty$ . Using (33) along with the bounding arguments in (31), it can be proved that the controller developed in (17) globally exponentially regulates the robot end-effector such that

$$\|e_\omega(t)\| \leq \left(\frac{\lambda_2}{\lambda_1}\right)^{1/2} \|e_\omega(0)\| \exp\left\{\frac{-k_{p\omega}}{2\lambda_2(1+k_{d\omega})} t\right\}. \quad (34)$$

The result in (29) can now be directly obtained from (34). Thus, the angular velocity control input in (17) ensures uniform global exponential regulation of robot end-effector such that the target fruit becomes visible to the CiH.  $\square$

### 5.2. Translation controller

**Theorem 2.** The translation velocity control input  $v_{cz}(t)$  in (21) ensures global exponential regulation of robot end-effector to the desired fruit depth in the sense that

$$\|e_{v2}(t)\| = \zeta_2 \exp\{-\zeta_3 t\} \quad (35)$$

where  $\zeta_2, \zeta_3 \in \mathbb{R}$  denote positive bounding constants.

**Proof.** Consider a positive definite Lyapunov function  $V_2(t)$  as

$$V_2 = \frac{1}{2} e_{v2}^T e_{v2} \quad (36)$$

$$\lambda_3 \|e_{v2}(t)\|^2 \leq V_2(t) \leq \lambda_4 \|e_{v2}(t)\|^2 \quad (37)$$

where  $\lambda_3, \lambda_4 \in \mathbb{R}$  are known positive bounding constants. Taking the time derivative of (36) and using (21) along with the fact that  $\dot{e}_{v2} = \alpha v_{cz}$ , the solution can be expressed in terms of the following inequality:

$$V_2(t) \leq V_2(0) \exp\left\{\frac{-\alpha k_{pv2}}{\lambda_4(1+\alpha k_{dv2})} t\right\}. \quad (38)$$

Using signal chasing arguments similar to presented in Section 5.1, it can be shown that  $e_{v2}(t), v_{cz}(t), \dot{e}_{v2}(t) \in \mathcal{L}_\infty$ . Using (38) along with the bounding arguments in (37), it can be proved that the control input  $v_{cz}(t)$  ensures uniform global exponential regulation of the end-effector to the desired depth such that

$$\|e_{v2}(t)\| \leq \left(\frac{\lambda_4}{\lambda_3}\right)^{1/2} \|e_{v2}(0)\| \exp\left\{\frac{-\alpha k_{pv2}}{2\lambda_4(1+\alpha k_{dv2})} t\right\}. \quad (39)$$

The result in (40) follows from (39).  $\square$

**Theorem 3.** The translation velocity control input  $v_{c1}(t)$  in (27) ensures global exponential regulation of target fruit image coordinates to the desired image coordinates in the sense that

$$\|e_{v1}(t)\| \leq \zeta_4 \exp\{-\zeta_5 t\} \quad (40)$$

where  $\zeta_4, \zeta_5 \in \mathbb{R}$  denote positive bounding constants.

**Proof.** Consider a positive definite Lyapunov function  $V_3(t)$  as

$$V_3 = \frac{1}{2} e_{v1}^T e_{v1} \quad (41)$$

$$\lambda_5 \|e_{v1}(t)\|^2 \leq V_3(t) \leq \lambda_6 \|e_{v1}(t)\|^2 \quad (42)$$

Taking the time derivative of (41) and substituting (21), (23), and (27), the expression for the Lyapunov derivative can be obtained as

$$\begin{aligned} \dot{V}_3 = & -\frac{\gamma k_{pv1}}{z} e_{v1}^T J'_v \zeta^{-1} e_{v1} - \frac{\gamma k'_{dv1} \chi}{z^2} e_{v1}^T J'_v \zeta^{-1} p_d e_{v2} \\ & + \frac{\gamma k'_{dv1} \chi}{z^2} e_{v1}^T J'_v \zeta^{-1} e_{v1} e_{v2} + \frac{\gamma \chi}{z} e_{v1}^T p_d e_{v2} - \frac{\gamma \chi}{z} e_{v1}^T e_{v1} e_{v2} \end{aligned} \quad (43)$$

where the facts that  $\dot{z}/z = \gamma$  and  $J''_v = p(t)$  are used. In (43),  $\chi \in \mathbb{R}_{>0}$  is a known constant given by  $\chi = (1 + \alpha k_{dv2})^{-1} k_{pv2}$  and the auxiliary signal  $\xi(t) \in \mathbb{R}$  is given by  $\xi = I_2 + \frac{k_{dv1}}{z} J'_v$ .

### Remark 2.

From the definition in (24), it can be seen that  $J'_v$  is a constant diagonal, positive definite matrix. Therefore, the auxiliary signal  $\xi$  is globally invertible, and  $\xi^{-1}$  is a diagonal, positive definite matrix. Since  $J'_v$  and  $\xi^{-1}$  are diagonal matrices, the product  $J'_v \xi^{-1}$  is also a diagonal, positive definite matrix.

**Property 1.** Using Remark 2, the diagonal, positive definite matrix  $J'_v \xi^{-1}$  satisfies the following inequality

$$\eta_1 \|\rho\|^2 \leq \rho^T J_v' \xi^{-1} \rho \leq \eta_2 \|\rho\|^2 \quad (44)$$

where  $\eta_1, \eta_2 \in \mathbb{R}_{>0}$  are known constants.

Using [Property 1](#) and the fact that  $k_{pv1} = k_{pv11} + k_{pv12}$ , the Lyapunov derivative in [\(43\)](#) can be upper bounded as

$$\begin{aligned} \dot{V}_3 \leq & -\frac{\eta_1 \gamma k_{pv11}}{\hat{z}(0)} \|e_{v1}\|^2 \\ & - \left[ \frac{\eta_1 \gamma k_{pv12}}{\hat{z}(0)} \|e_{v1}\|^2 - \frac{\eta_2 \alpha^2 \gamma k_{dv1} \chi}{z_d^2} \|e_{v1}\|^2 \|e_{v2}\| - \frac{\alpha \gamma \chi}{z_d} \|e_{v1}\|^2 \|e_{v2}\| \right. \\ & \left. - \left( \frac{\alpha^2 \gamma k_{dv1} \chi}{z_d^2} \|J_v'\| \xi^{-1} \|p_d\| \|e_{v2}\| + \frac{\alpha \gamma \chi}{z_d} \|p_d\| \|e_{v2}\| \right) \|e_{v1}\| \right] \quad (45) \end{aligned}$$

where  $\hat{z}(0) \in \mathbb{R}$  is the estimated depth of the fruit at  $t = 0$  which, using [\(39\)](#), represents an upper bound on  $\hat{z}(t)$ , and  $\lim_{t \rightarrow \infty} \hat{z}(t) = z_d/\alpha$  is the lower bound on  $\hat{z}(t)$ . Completing the squares on the bracketed terms yields the following inequality:

$$\begin{aligned} \dot{V}_3 \leq & -\frac{\eta_1 \gamma k_{pv11}}{\hat{z}(0)} \|e_{v1}\|^2 - \frac{\gamma \Gamma(e_{v2})}{\hat{z}(0) z_d^2} \left[ \|e_{v1}\|^2 \right. \\ & - \left( \frac{\alpha^2 k_{dv1} \chi \hat{z}(0)}{\Gamma(e_{v2})} \|J_v'\| \xi^{-1} \|p_d\| \|e_{v2}\| + \frac{\alpha \chi \hat{z}(0) z_d}{\Gamma(e_{v2})} \|p_d\| \|e_{v2}\| \right) \|e_{v1}\| \\ & + \left( \frac{\alpha^2 k_{dv1} \chi \hat{z}(0)}{2 \Gamma(e_{v2})} \|J_v'\| \xi^{-1} \|p_d\| \|e_{v2}\| + \frac{\alpha \chi \hat{z}(0) z_d}{2 \Gamma(e_{v2})} \|p_d\| \|e_{v2}\| \right)^2 \Big] \\ & + \frac{\gamma \hat{z}(0)}{4 \Gamma(e_{v2}) z_d^2} \left( \alpha^2 k_{dv1} \chi \|J_v'\| \xi^{-1} \|p_d\| \|e_{v2}\| + \alpha \chi z_d \|p_d\| \|e_{v2}\| \right)^2 \quad (46) \end{aligned}$$

where  $\Gamma(e_{v2}) = \eta_1 k_{pv12} z_d^2 - \eta_2 \alpha^2 k_{dv1} \chi \hat{z}(0) \|e_{v2}\| - \alpha \chi z_d \hat{z}(0) \|e_{v2}\|$  is an auxiliary function for which positive definiteness can be guaranteed with the following gain condition:

$$k_{pv1} > \frac{\eta_2 \alpha^2 k_{dv1} \chi \hat{z}(0) + \alpha \chi z_d \hat{z}(0)}{\eta_1 z_d^2} \|e_{v2}(0)\|. \quad (47)$$

Consequently, for all  $(e_{v1}, t) \in \mathbb{R}^3 \times \mathbb{R}$ , [\(42\)](#) can be used to express inequality [\(46\)](#) as

$$\dot{V}_3 \leq -\frac{\eta_1 \gamma k_{pv11}}{\lambda_6 \hat{z}(0)} V_3(t) + \beta \quad (48)$$

where  $\beta(e_{v2})$  is the following positive, bounded function:

$$\begin{aligned} \beta &= \frac{\gamma \hat{z}(0)}{4 z_d^2} \left( \alpha^2 k_{dv1} \chi \|J_v'\| \xi^{-1} \|p_d\| + \alpha \chi z_d \|p_d\| \right)^2 \frac{\|e_{v2}\|^2}{\Gamma(e_{v2})} \\ &= \delta \frac{\|e_{v2}\|^2}{\Gamma(e_{v2})}. \quad (49) \end{aligned}$$

In [\(49\)](#),  $\delta \in \mathbb{R}_{>0}$  denotes a constant. The expressions in [\(41\)](#), [\(42\)](#), and [\(48\)](#) can be used to conclude that  $e_{v1}(t) \in \mathcal{L}_\infty$ . Given that  $e_{v1}(t) \in \mathcal{L}_\infty$  and from [\(39\)](#)  $e_{v2}(t) \in \mathcal{L}_\infty$ , [\(23\)](#) and [\(27\)](#) can be used to conclude that  $v_{c1}(t) \in \mathcal{L}_\infty$  and  $\dot{e}_{v1}(t) \in \mathcal{L}_\infty$ . The expression in [\(39\)](#) can be used to solve for [\(48\)](#) as

$$V_3(t) \leq \frac{\zeta_4^2}{2} \exp\{-2\zeta_5 t\}. \quad (50)$$

The expression in [\(41\)](#) and inequality in [\(50\)](#) can be used to conclude that

$$\|e_{v1}(t)\|^2 \leq \zeta_4^2 \exp\{-2\zeta_5 t\} \quad (51)$$

The result in [\(40\)](#) can now be directly obtained from [\(51\)](#). Thus, the translation control input designed in [\(27\)](#) guarantees uniform global exponential regulation of target fruit image coordinates to the desired image coordinates.  $\square$

## 6. Simulation results

A numerical simulation was performed to demonstrate the feasibility of the proposed controller for citrus harvesting. The initial position  $t_r \in \mathbb{R}^3$  and orientation  $R_r \in \mathbb{R}^{3 \times 3}$  of the CiH coordinate frame  $\mathcal{F}$  with respect to  $\mathcal{F}_b$  was considered to be

$$t_r = [20 \ 60 \ 1500]^T \text{ mm}, \quad R_r = \begin{bmatrix} 0.4698 & -0.1955 & 0.8608 \\ 0.1710 & 0.9769 & 0.1285 \\ -0.8660 & 0.0868 & 0.4924 \end{bmatrix}. \quad (52)$$

The simulation was repeated for three different fruit locations given below. Since the goal is to verify the feasibility of the developed controller, instead of using [\(6\)](#) and [\(7\)](#), the simulation results assume the estimated position of the target fruits  $\hat{m}_b$  in  $\mathcal{F}_b$  with  $\approx 2\%$  depth estimation error as

$$O^* = [525 \ 375 \ 2450]^T \text{ mm}, \quad \hat{m}_b = [500 \ 400 \ 2500]^T \text{ mm}, \quad (53)$$

$$O^* = [190 \ 295 \ 1860]^T \text{ mm}, \quad \hat{m}_b = [200 \ 300 \ 1900]^T \text{ mm}, \quad (54)$$

$$O^* = [375 \ 35 \ 2155]^T \text{ mm}, \quad \hat{m}_b = [400 \ 50 \ 2200]^T \text{ mm}. \quad (55)$$

Let the constant camera calibration matrix  $A$  be as follows:

$$A = \begin{bmatrix} 7000 & 0 & 320 \\ 0 & 7000 & 240 \\ 0 & 0 & 1 \end{bmatrix} \quad (56)$$

and the fruit pixel coordinates were assumed to be affected by zero-mean Gaussian noise of standard deviation 0.5 pixel. Note that the calibration matrix  $A_f$  is not required for numerical simulations since the fruit already is assumed to be detected with certain depth estimation error. Various control gains were selected as follows:

$$k_{p\omega} = 8, \quad k_{d\omega}, \quad k_{dv1} = 0.1, \quad k_{pv1} = 10, \quad k_{pv2} = 1, \quad k_{dv2} = 0.4. \quad (57)$$

[Fig. 2](#) shows the time-varying trajectory of the robot end-effector during rotation and translation control along with the target fruit positions. The CiH image-space trajectory of the target fruit is shown in [Fig. 3](#). In [Fig. 3](#), the solid lines represent the

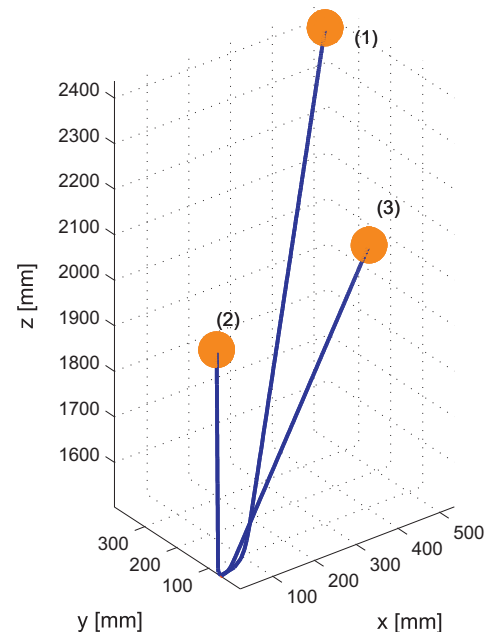


**Fig. 2.** Euclidean plot showing the target fruits and the end-effector trajectory.

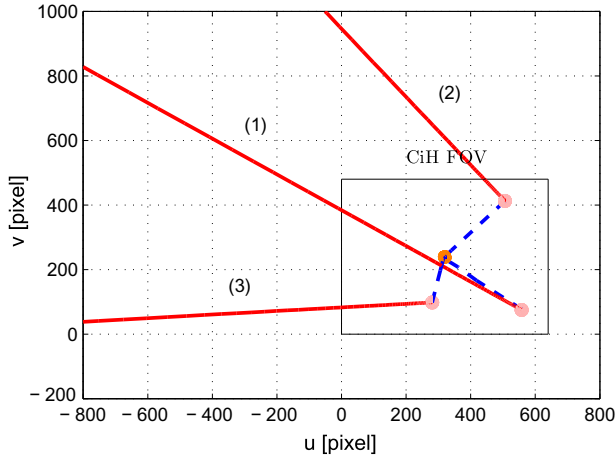


**Fig. 3.** The solid lines represent the image-space trajectory of the fruits during rotation control to bring the fruit in the CiH FOV, while the dashed lines show the fruit coordinates during translation control, where  $p_d = [320 \ 240]^T$ .

image-space position of the fruits during rotation control to bring the fruit in the FOV of the CiH. At the end of rotation control the target fruit is guaranteed to be in the FOV but not necessarily at the center of image due to discrepancies between  $O^*$  and  $\hat{m}_b$  in (53)–(55). The dashed lines in Fig. 3 represent the image-space trajectories of the target fruits during translation control to regulate the image coordinates to  $p_d = [320 \ 240]^T$ . In Figs. 2 and 3, the trajectories denoted by (1), (2), and (3) correspond to the fruit positions in (53)–(55), respectively. The rotation error and angular velocity plots are shown in Figs. 4 and 6, respectively, while Figs. 5 and 7 shows the translation errors and linear velocities of the end-effector, respectively. In Figs. 4–7, the solid line corresponds to the fruit in (53), the dashed lines indicate the fruit in (54), and the dashed-dotted lines are for the fruit in (55). It can be seen from Figs. 4 and 5 that the rotation and translation errors exponentially decrease to zero, while the angular and linear velocities in Figs. 6 and 7 are always bounded.

## 7. Experimental validation

The proposed cooperative visual servo controller is experimentally evaluated to determine feasibility for robotic citrus harvesting. A preliminary study was carried out to verify the

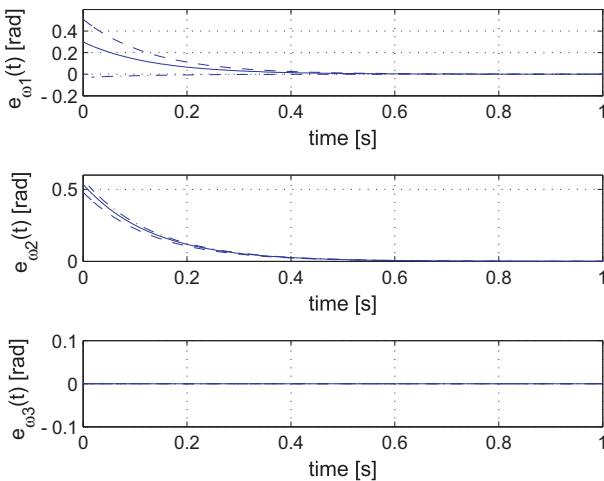


**Fig. 4.** Rotation error  $e_{\omega}(t) = [e_{\omega 1}(t) \ e_{\omega 2}(t) \ e_{\omega 3}(t)]^T$ .

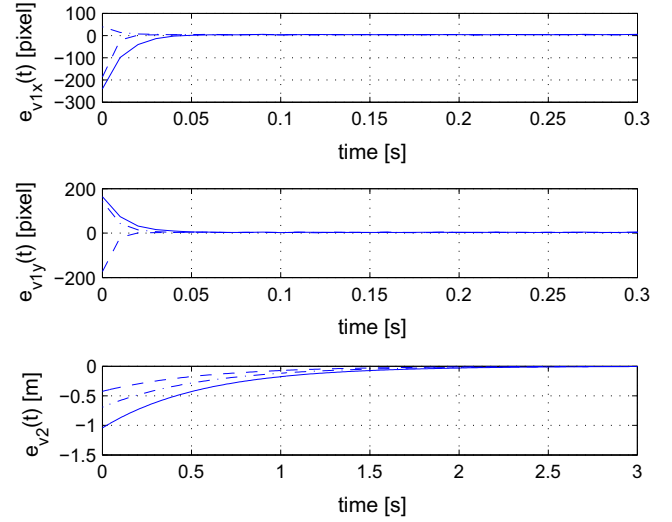


**Fig. 5.** Translation error  $e_v(t) = [e_{v1}^T(t) \ e_{v2}(t)]^T$ , where  $e_{v1}(t) = [e_{v1x}(t) \ e_{v1y}(t)]^T$ .

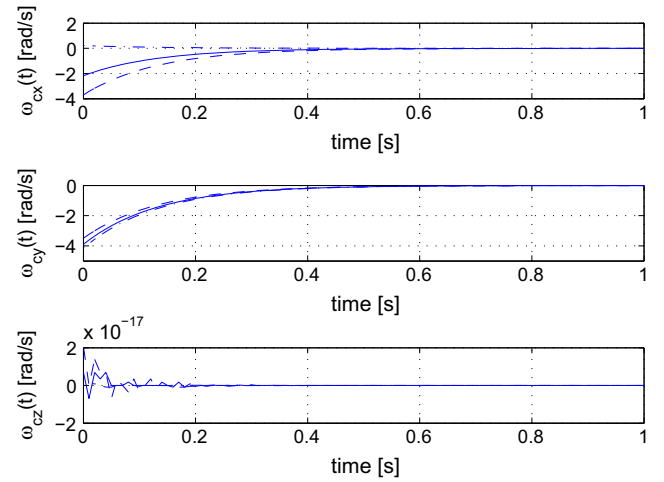


**Fig. 6.** Angular velocity  $\omega_c(t) = [\omega_{\alpha}(t) \ \omega_{\gamma}(t) \ \omega_{\zeta}(t)]^T$ .

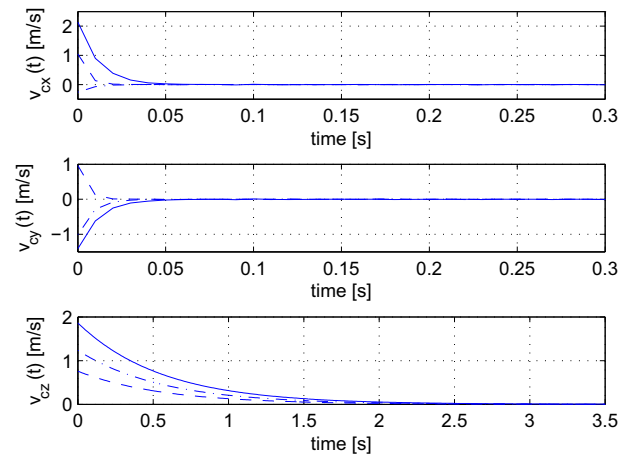


**Fig. 7.** Linear velocity  $v_c(t) = [v_{cx}(t) \ v_{cy}(t) \ v_{cz}(t)]^T$ .

performance of the depth estimation method presented in Section 2. Incorporating findings from the preliminary study an experiment was conducted to evaluate the feasibility of the controller using a seven DOF robotic manipulator.

### 7.1. Performance of the depth estimator

In this section, the performance of the Euclidean depth estimator presented in (6) and (7) is verified using an experiment. A color CCD camera (KT&C, KPCS20-CP1) with focal length of 4.3 mm and resolution of  $640 \times 480$  was used to capture the images of a citrus fruit. The NTSC analog output from the camera was digitized using a USB frame grabber. Image processing and depth estimation were performed on a computer with 3.06 GHz Intel Pentium 4 processor and 764 Mb RAM.

For the given citrus variety, the sample mean major and minor axes of the fruit were observed to be  $d_{ox} = 74.99$  mm and  $d_{oy} = 77.31$  mm, respectively. The camera was calibrated using Caltech Camera Calibration Toolbox to obtain the calibration parameters given in (5). The product of the focal length and camera scaling factors were observed to be  $\lambda_x f = 833.57$  pixels, and  $\lambda_y f = 767.02$  pixels. The performance of the depth estimator was evaluated by varying the distance of the camera from the fruit. During the experiment, the position of the fruit was kept stationary while the camera was displaced in the increments of 100 mm along the direction of fruit. Color thresholding-based algorithm was developed to detect the fruit in the scene and evaluate the pix-

el area  $A_p$ . Using (6), the fruit depth was estimated at each camera position. The estimation error was computed as the percentage discrepancy between the actual depth (measured) and the estimated depth.

The results of depth estimation are provided in Fig. 8 that shows the plot of the depth estimation error as a function of distance between the fruit and the camera. It can be seen from Fig. 8 that the depth estimator exhibits small error ( $< 2\%$ ) for camera distance greater than 450 mm. Estimation error of this magnitude is observed to have no detrimental effect on the performance of the rotation controller in (14) that relies on  $\hat{z}_f$  from the fixed camera. Therefore, in the presented cooperative vision system, the fixed camera is mounted at a distance  $\geq 450$  mm from the tree canopy. It is to be noted that the acceptable estimation error depends on the FOV of the CiH in the sense that large FOV can tolerate more estimation errors since the fruit can still be maintained in the FOV.

### 7.2. Performance of the visual servo controller

The performance of the proposed visual servo controller was demonstrated using a 7 DOF Robotics Research K1207 manipulator shown in Fig. 9. The indoor experiment comprised of a synthetic citrus tree and two color CCD cameras (KT&C, KPCS20-CP1) with focal length of 4.3 mm and resolution of  $640 \times 480$  that served as the fixed camera and the CiH. The fixed camera was mounted on stationary base of the manipulator as shown in Fig. 9a while the CiH was attached to the robot end-effector as shown in Fig. 9b. Images from both the cameras were digitized using USB frame grabbers. The image processing workstation (IPW) was used to identify fruits from the captured images using the method described in Hannan et al. (2009), and the Euclidean position of the identified fruits was estimated with respect to  $\mathcal{F}_f$  and  $\mathcal{F}$  using the developed perspective transformation based range estimation method in (6) and (7). Based on the obtained fruit position, the rotation (14) and, subsequently, the translation control input in (21) and (27) was generated to regulate the end-effector to the fruit position. The robot control workstation (RCW) hosted a lower level controller to generate joint torque commands based on the control input from IPW. Also, the RCW broadcasted the joint position feedback along with the end-effector position and orientation to the IPW through a real-time communication network.

The rotation and translation vectors of the extrinsic camera calibration matrix  $A_{ef}$  in (9) for the fixed camera was measured to be

$$R_{ef} = \begin{bmatrix} 0 & 0 & -1 \\ 1 & 0 & 0 \\ 0 & 1 & 0 \end{bmatrix} \quad t_{ef} = \begin{bmatrix} 254.00 \\ -196.85 \\ 381.00 \end{bmatrix}. \quad (58)$$

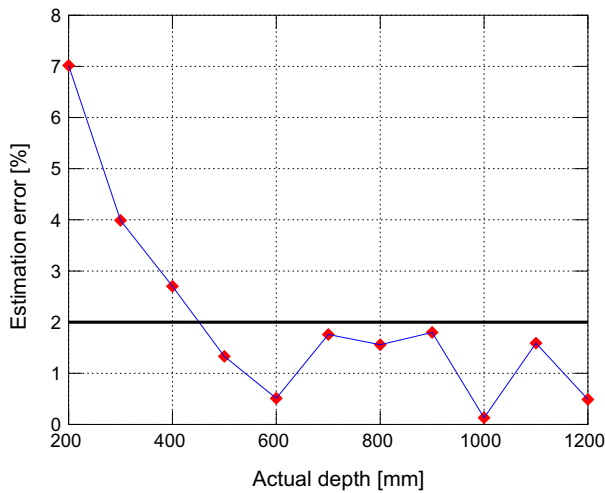


Fig. 8. Estimation error as a function of the actual camera-to-fruit depth.

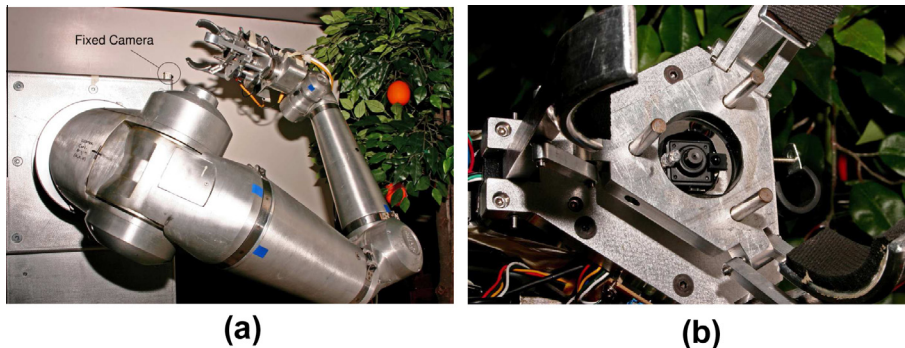


Fig. 9. (a) Robotic Research K1207 manipulator with the fixed camera mounted on the stationary base of the robot and (b) the CiH located inside the robot end-effector.



**Table 1**

Initial  $\mathcal{F}(0)$  and final  $\mathcal{F}(n)$  position of CiH coordinate frame  $\mathcal{F}$  and target fruit position  $O^*$  measured in base frame  $\mathcal{F}_b$ .

		Initial position $\mathcal{F}(0)$ (mm)	Final position $\mathcal{F}(n)$ (mm)	Fruit position $O^*$ (mm)	Error (mm)
1	x	549.0	−75.0	−68.6	12.310
	y	896.0	1180.0	1174.4	
	z	−203.0	−384.0	−375.1	
2	x	40.0	−63.0	−68.6	15.503
	y	979.0	1188.0	1174.4	
	z	61.0	−380.0	−375.1	
3	x	−715.0	−63.0	−68.6	12.583
	y	748.0	1184.0	1174.4	
	z	47.0	−381.0	−375.1	
4	x	−138.0	−272.0	−266.7	22.714
	y	1015	998.0	1016.0	
	z	−223	−553.0	−540.2	
5	x	−538.0	−235.0	−228.6	22.606
	y	554.0	1048.0	1066.8	
	z	−920.0	−451.0	−440.2	
6	x	39.0	−416.0	−412.6	24.697
	y	981.0	992.0	1011.4	
	z	69.0	−514.0	−528.9	
7	x	−655.0	−238.0	−228.6	23.140
	y	785.0	1123.0	1126.8	
	z	−251.0	−561.0	−540.2	
8	x	−655.0	−234.0	−228.6	11.119
	y	785.0	1121.0	1126.8	
	z	−251.0	−548.0	−540.2	
9	x	−655.0	−215.0	−228.6	25.566
	y	785.0	1111.0	1126.8	
	z	−251.0	−555.0	−540.2	
10	x	−655.0	−226.0	−228.6	11.681
	y	785.0	1117.0	1126.8	
	z	−251.0	−546.0	−540.2	
11	x	−655.0	−227.0	−228.6	11.935
	y	785.0	1115.0	1126.8	
	z	−251.0	−541.0	−540.2	
12	x	−655.0	−227.0	−228.6	9.1236
	y	785.0	1118.0	1126.8	
	z	−251.0	−542.0	−540.2	
13	x	−655.0	−228.0	−228.6	11.047
	y	785.0	1119.0	1126.8	
	z	−251.0	−548.0	−540.2	
14	x	−655.0	−229.0	−228.6	14.058
	y	785.0	1114.0	1126.8	
	z	−251.0	−546.0	−540.2	
15	x	−655.0	−226.0	−228.6	13.865
	y	785.0	1120.0	1126.8	
	z	−251.0	−552.0	−540.2	
16	x	−655.0	−229.0	−228.6	15.279
	y	785.0	1116.0	1126.8	
	z	−251.0	−551.0	−540.2	
17	x	−655.0	−219.0	−228.6	24.687
	y	785.0	1108.0	1126.8	
	z	−251.0	−553.0	−540.2	
18	x	−655.0	−230.0	−228.6	8.9129
	y	785.0	1118.0	1126.8	
	z	−251.0	−540.0	−540.2	
19	x	−655.0	−220.0	−228.6	21.919
	y	785.0	1107.0	1126.8	
	z	−251.0	−544.0	−540.2	
20	x	−655.0	−214.0	−228.6	26.307
	y	785.0	1106.0	1126.8	
	z	−251.0	−547.0	−540.2	
21	x	−655.0	−231.0	−228.6	11.834
	y	785.0	1116.0	1126.8	
	z	−251.0	−536.0	−540.2	

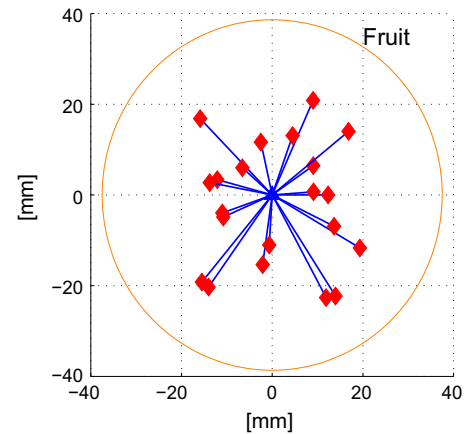


**Fig. 10.** Plot showing Euclidean distance error between the final position of CiH  $\mathcal{F}(n)$  (red  $\diamond$ ) and the fruit centroid  $O^*$  (blue  $\triangle$ ) for the obtained 21 observations. (For interpretation of the references to color in this figure legend, the reader is referred to the web version of this article.)

Similarly, the extrinsic camera calibration parameters for the CiH were observed to be<sup>3</sup>

$$R_e = \begin{bmatrix} 1 & 0 & 0 \\ 0 & -1 & 0 \\ 0 & 0 & 1 \end{bmatrix} \quad t_e = \begin{bmatrix} 0 \\ 0 \\ 190.5 \end{bmatrix}. \quad (59)$$

In (58) and (59),  $\det(R_{ef}), \det(R_e) \neq 1$ , since these improper rotations include the coordinate transformation matrix between the left-handed camera coordinate frame and the right-handed robot coordinate frame. However, note that  $R_{ef}^{-1} = R_{ef}^T$  and  $R_e^{-1} = R_e^T$ , and hence the results in (14) and (28) are valid. An infrared proximity sensor was used to detect the presence of fruit and activate the gripper mechanism. The fruit can then be detached by executing a predefined trajectory.

Table 1 presents the result of visual servo controller developed in (14), (21), and (27), where  $\mathcal{F}(0) = \mathcal{F}(t)|_{t=0}$  and  $\mathcal{F}(n) = \mathcal{F}(t)|_{t=n}$  denote the initial and final position, respectively, of the CiH frame  $\mathcal{F}$  with respect to  $\mathcal{F}_b$ . The experiment was repeated several times for different robot and fruit positions. The actual fruit position  $O^*$  was measured using forward kinematic analysis by positioning the end-effector at the center of the fruit. Fig. 10 shows the polar plot of the Euclidean distance error between  $\mathcal{F}(n)$  (red  $\diamond$ ) and  $O^*$  (blue  $\triangle$ ). To assist in visualizing the results, the fruit is shown as an ellipse of axes  $\{d_{ox}, d_{oy}\}$ . From the fact that regulation error is less than the radius of the fruit and that the fruit was harvested successfully during each trial, the preliminary results indicate satisfactory performance of the developed visual servo controller.

### 7.3. Repeatability and accuracy

The repeatability of a positioning system is the extent to which successive attempts to move to a specific location vary in position. A highly repeatable system exhibits very low scatter in repeated moves to a given position under the same conditions. While the accuracy is defined in terms of the degree of closeness of measurements to its true value.

The repeatability and accuracy of the proposed controller were examined by servoing the manipulator from an identical initial position  $\mathcal{F}(0)$  to the same desired position  $O^*$ . The experiment was repeated 15 times and the final position  $\mathcal{F}(n)$  was recorded for each

<sup>3</sup> The extrinsic camera calibration parameters  $\{R_{ef}, t_{ef}\}$  in (58) and  $\{R_e, t_e\}$  in (59) are obtained using commercial grade digital level and laser range finder, respectively, within the accuracy of the sensors.

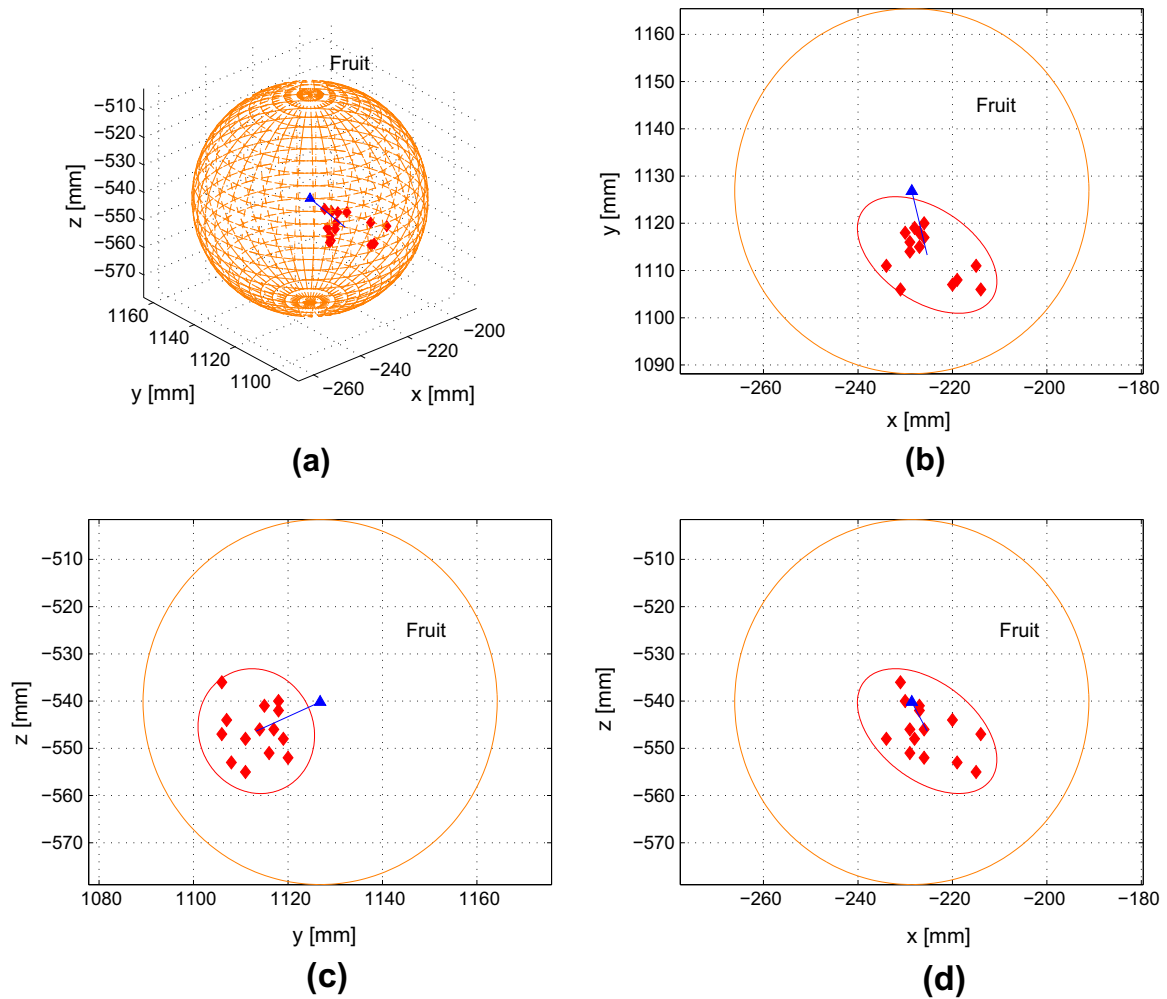


**Fig. 11.** Repeatability and accuracy of the proposed visual servo controller: (a) Euclidean plot showing the final position of the CiH frame  $\mathcal{F}(n)$  (red  $\diamond$ ) and the fruit centroid (blue  $\triangle$ ) along with the fruit; (b, c, and d) 2D plots in  $xy$ ,  $yz$ , and  $xz$ -plane, respectively, showing a 95% confidence covariance ellipsoid of final position  $\mathcal{F}(n)$ , which indicates the repeatability of the controller. The accuracy is expressed as the Euclidean distance between the observations and the fruit center that is observed to be  $a_{xy} = 13.898$  mm,  $a_{yz} = 14.851$  mm, and  $a_{xz} = 6.9589$  mm in the  $xy$ ,  $yz$ , and  $xz$ -plane, respectively, and  $a_{xyz} = 15.201$  mm in the 3D coordinate frame. (For interpretation of the references to color in this figure legend, the reader is referred to the web version of this article.)

experiment. The set of observations obtained during the repeated moves are shown in Table 1 (observations 7–21).

The results of the experiment are shown in Fig. 11. Fig. 11a shows the Euclidean position of the CiH frame  $\mathcal{F}(n)$  (red  $\diamond$ ) during repeated moves along with fruit centroid  $O^*$  (blue  $\triangle$ ). As it can be observed from Fig. 11a, the regulation error is always less than the size of the fruit. Fig. 11b–d show the position of  $\mathcal{F}(n)$  and  $O^*$  in  $xy$ ,  $yz$ , and  $xz$ -plane, respectively. A 95% confidence covariance ellipsoid is shown such that with 95% confidence level the expected position of  $\mathcal{F}_n$  lies within the confidence ellipsoid for each case. The major and minor axes of the ellipsoids for the three cases are as follows (in mm):  $xy$ -plane {31, 19.6},  $yz$ -plane {24.2, 26.8}, and  $xz$ -plane {33.8, 20.4}. It can be seen from Fig. 11b–d that the ellipsoid in each case is much smaller than the fruit, and hence the repeatability of the controller is considered to be satisfactory.

The accuracy is measured in terms of the Euclidean distance between the observations and the fruit centroid. From Fig. 11, the accuracy is observed to be  $a_{xy} = 13.898$  mm,  $a_{yz} = 14.851$  mm, and  $a_{xz} = 6.9589$  mm in the  $xy$ ,  $yz$ , and  $xz$ -plane, respectively, and  $a_{xyz} = 15.201$  mm in the 3D coordinate frame. Considering the fact that the fruit was harvested successfully each time and that  $\{a_{xy}, a_{yz}, a_{xz}\} \ll \{d_{ox}, d_{oy}\}$ , we conclude that the obtained accuracy is sufficient for citrus harvesting. The repeatability and accuracy

of the developed system depends on the fruit size. With an accuracy of  $\approx 15$  mm, the system is suitable for harvesting medium and large varieties of citrus fruit, and may limit operation for small varieties such as page and blood oranges.

## 8. Conclusion

The unknown fruit depth from the camera is estimated using computationally simple perspective transformation rather than relying on cumbersome stereo-vision or triangulation schemes. A cooperative visual servo controller is presented for robotic fruit harvesting. An in-depth control development and Lyapunov-based stability analysis is presented that guarantees global exponential regulation of the end-effector to the target fruit position. The developed estimation and control methods can easily be extended to other fruits with general ellipsoid geometry. Experimental results on seven degrees-of-freedom robotic manipulator using an artificial citrus tree indicate satisfactory performance, where the robot consistently picked fruits attached randomly to the tree using the proposed controller. Future research will consider advanced robust and adaptive nonlinear control systems to compensate for the unknown fruit motion due to wind gusts and robot-tree contact and the unmodeled robot dynamics.

## Appendix A. Field challenges

In this section, various challenges pertaining to an actual system and the corresponding merits and demerits of the developed controller are identified. Open problems and the scope for future work is also discussed.

### A.1. Illumination, shadows, partial occlusion

Environmental factors such as uneven illumination, shadows cast by branches and leaves, and partial fruit occlusion can lead to partial fruit detection, where only a part of the fruit is identified. Moreover, the centroid of the partially detected fruit in the camera image plane may not coincide with the true centroid (i.e.,  $p_f \neq p_{f_{true}}$  and  $p \neq p_{true}$ ). A brief analysis is presented below to discuss robustness characteristics of the developed visual servo controller to the fruit detection errors.

Due to partial detection, let the true and the measured area of a fruit in the camera image plane be denoted by  $A_{p_{true}} \in \mathbb{R}$  and  $A_p$ , respectively, where  $A_{p_{true}} \geq A_p$  or  $A_{p_{true}} = \gamma_A A_p$  for  $\gamma_A \geq 1$ . From (6) and (7), it can be shown that the estimated depth  $\hat{z}_f = \sqrt{\gamma_A} z_{f_{true}}$ . Let  $\gamma_z = \sqrt{\gamma_A}$  be the depth uncertainty resulting from partial detection. Now, due to partial fruit detection, the error in the position of the measured fruit centroid can be quantified as

$$\begin{bmatrix} p_f^T & 1 \end{bmatrix}^T = \begin{bmatrix} \gamma_x & 0 & 0 \\ 0 & \gamma_y & 0 \\ 0 & 0 & 1 \end{bmatrix} \begin{bmatrix} p_{f_{true}}^T & 1 \end{bmatrix}^T \quad (\text{A.1})$$

where  $\gamma_x, \gamma_y \in \mathbb{R}_{>0}$  represent position uncertainties in the fruit image coordinates. Using (A.1) and (8), the relationship between the estimated,  $\hat{m}_f$ , and the true,  $\bar{m}_{f_{true}}$ , fruit position in the fixed camera frame can be obtained as

$$\hat{m}_f = A_f^{-1} \begin{bmatrix} \gamma_x & 0 & 0 \\ 0 & \gamma_y & 0 \\ 0 & 0 & 1 \end{bmatrix} \begin{bmatrix} p_{f_{true}}^T & 1 \end{bmatrix}^T \hat{z}_f = A_f^{-1} \underbrace{\begin{bmatrix} \gamma_x \gamma_z & 0 & 0 \\ 0 & \gamma_y \gamma_z & 0 \\ 0 & 0 & \gamma_z \end{bmatrix}}_{\gamma_u} A_f \bar{m}_{f_{true}} \quad (\text{A.2})$$

where the fact that  $\hat{z}_f = \gamma_z z_{f_{true}}$  is used. Substituting (A.2) in (9) and using (12), the estimated fruit position in the CiH coordinate frame  $\mathcal{F}$  can be obtained as

$$\hat{m}'(t) = R_r^{-1} \left( R_{ef} A_f^{-1} \gamma_u A_f \bar{m}_{f_{true}} + t_{ef} - t_r \right). \quad (\text{A.3})$$

#### A.1.1. Rotation controller

At this point, we are interested in finding whether in the presence of uncertainty  $\gamma_u$  the target fruit can be visible to the CiH after rotation control. Since the objective of the rotation control is to regulate the estimated fruit position  $\hat{m}'(t)$  to the center of the CiH, we have

$$\bar{m}_{f_{true}} = A_f^{-1} \gamma_u^{-1} A_f R_{ef}^{-1} \left( R_r \begin{bmatrix} 0 & 0 & \hat{z}' \end{bmatrix}^T - t_{ef} + t_r \right). \quad (\text{A.4})$$

Therefore, the true position,  $\bar{m}_{true}(t)$ , of the fruit in the CiH coordinate frame at the end of rotation control can be obtained as

$$\bar{m}_{true}(t) = R_r^{-1} \left( R_{ef} A_f^{-1} \gamma_u^{-1} A_f R_{ef}^{-1} \left( R_r \begin{bmatrix} 0 & 0 & \hat{z}' \end{bmatrix}^T - t_{ef} + t_r \right) + t_{ef} - t_r \right). \quad (\text{A.5})$$

It can be verified that in the absence of uncertainty, i.e.,  $\gamma_u = I_3$ , the true and the estimated positions coincide, i.e.,  $\bar{m}_{true}(t) = \hat{m}'(t) = \begin{bmatrix} 0 & 0 & \hat{z}' \end{bmatrix}^T$ . From (A.5), the image coordinates,  $p_{true}(t)$ , corresponding to  $\bar{m}_{true}(t)$  can be obtained as

$$p_{true}(t) = \frac{1}{z_{true}} A \bar{m}_{true}(t). \quad (\text{A.6})$$

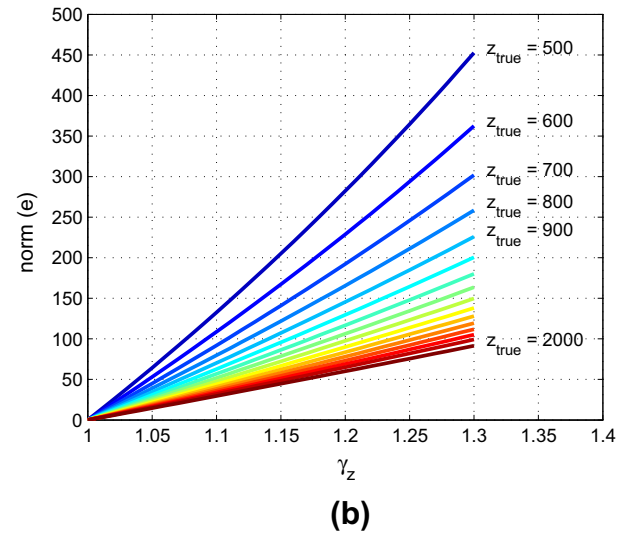
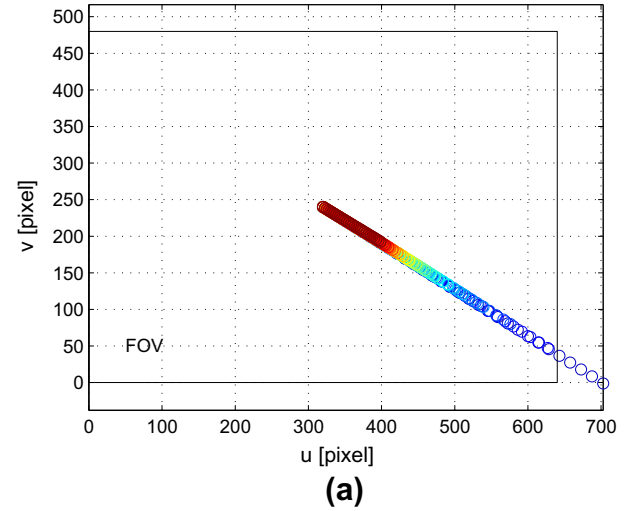


**Fig. A.12.** (A) The true image coordinates  $p_{true}$  of a fruit as a function of depth uncertainty  $\gamma_z$  for various fruit depths; (B) deviation in the true image coordinates,  $p_{true}$ , from the image center.

where  $z_{true} \in \mathbb{R}$  is the depth of the CiH from the fruit after rotation control. From (A.6), it can be seen that any deviation in  $\bar{m}_{true}(t)$  from  $\hat{m}'(t)$  due to uncertainties  $\gamma_u$  results in the deviation of  $p_{true}(t)$  from the image center. However, for the CiH to view the fruit the image coordinates  $p_{true}(t)$  are only required to lie in the FOV of the CiH, therefore, the rotation controller is inherently tolerant to uncertainties due to partial fruit detection. It can be seen from (A.6) that the robustness depends on the camera calibration parameters,  $A$ , of the CiH, such that the robustness can be improved by selecting a camera with short focal length (i.e., wide FOV).

To demonstrate the robustness of the developed rotation controller consider an example where the depth uncertainty  $\gamma_z$  due to partial fruit detection vary between 1.0 and 1.3, i.e., up to about 40% of the fruit may not be detected. Since in (A.6) the image coordinates  $p_{true}$  are functions of the fruit depth,  $z_{true}$  is varied from 500 to 2000 mm. The results are shown in Fig. A.12; Fig. A.12A shows the true image position  $p_{true}$  of the fruit as a function of  $\gamma_z$  for various fruit depths  $z_{true}$ ; Fig. A.12B shows the deviation of  $p_{true}$  from the image center, where the error  $e(t)$  is defined as  $e \triangleq p_d - p_{true}$ .

In the second example, the depth uncertainty is kept constant at  $\gamma_z = 1.2$ , and the uncertainty in the of fruit centroid,  $\gamma_x$  and  $\gamma_y$ , is varied between 0.8 and 1.2. The results are shown in Fig. A.13;

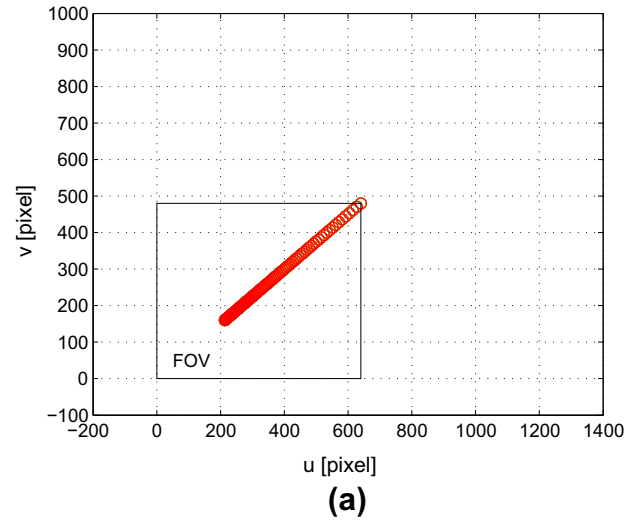
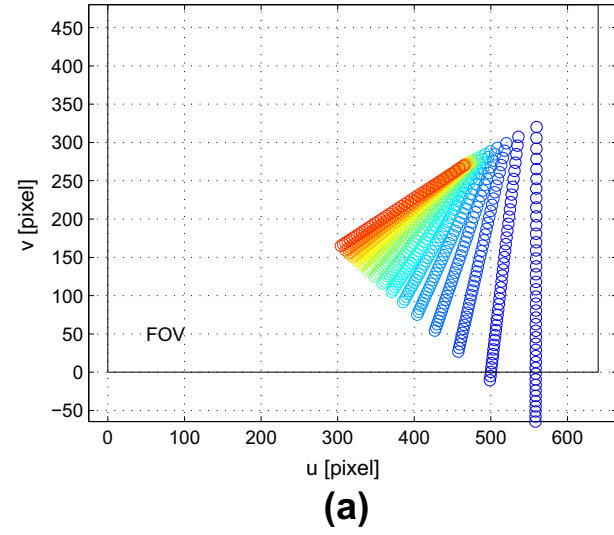


**Fig. A.13.** (A) The true image coordinates  $p_{\text{true}}$  of a fruit as a function of  $\gamma_x$  and  $\gamma_y$  for various fruit depths; (B) deviation in the true image coordinates,  $p_{\text{true}}$ , from the image center.

Fig. A.13A shows the image position  $p_{\text{true}}$  of the fruit as a function of  $\gamma_x$  and  $\gamma_y$  for various depths  $z_{\text{true}}$ ; Fig. A.13B shows the deviation of  $p_{\text{true}}$  from the image center.

It can be seen from Fig. A.13A that the fruit remains in the camera FOV for most  $\gamma_x, \gamma_y$ , and  $z_{\text{true}}$ . From Figs. A.12A and A.13A, the robustness of the rotation controller is observed to degrade with decrease in the initial fruit depth  $z_{\text{true}}$  of the CiH, which is evident from (A.6).

#### A.1.2. Translation controller

The developed image-based translation controller is robust to depth uncertainty  $\gamma_z$ . The translation error along the optical axis is defined in (19) as  $e_{v2} = z_d - \alpha \hat{z}$ , where  $\alpha$  is a constant design parameter that can be selected arbitrarily high to guarantee robustness with respect to depth estimation errors.

Let us analyze the effect of uncertainties  $\gamma_x$  and  $\gamma_y$  on the performance of the developed translation controller. The true normalized coordinates of the fruit centroid in the CiH coordinate frame  $\mathcal{F}$  are given by  $m_{\text{true}} = A^{-1}p_{\text{true}}$ . Using the definition of uncertainty given in (A.1), following expression can be obtained:

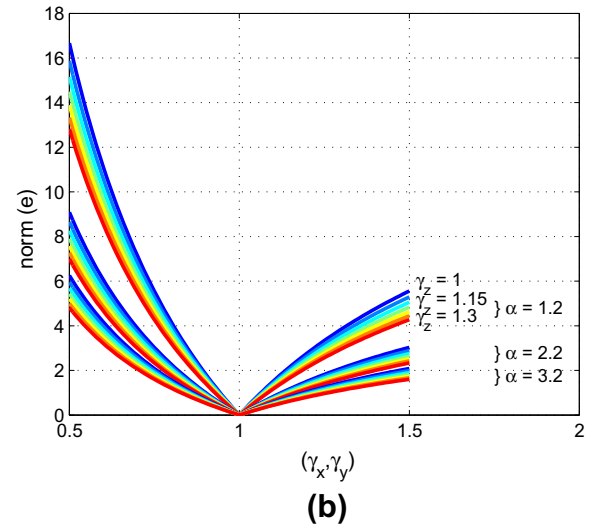


**Fig. A.14.** (A) The true image coordinates  $p_{\text{true}}$  of a fruit as a function of  $\gamma_x$ ,  $\gamma_y$ , and  $\gamma_z$ ; (B) deviation in the true fruit position  $\bar{m}_{\text{true}}$  from the servoed position.

$$\bar{m}_{\text{true}} = z_{\text{true}} A^{-1} \begin{bmatrix} \gamma_x & 0 & 0 \\ 0 & \gamma_y & 0 \\ 0 & 0 & 1 \end{bmatrix}^{-1} [p^T \ 1]^T. \quad (\text{A.7})$$

The translation control input  $v_{c1}(t)$  in (27) guarantees global exponential regulation of  $p(t)$  to constant  $p_d$ , while the control input  $v_{cz}(t)$  in (21) guarantees global exponential regulation of the end-effector such that  $\hat{z} = z_d/\alpha$  as  $t \rightarrow \infty$ . Therefore, after simplifying the expression in (A.7), the position of the fruit at the end of translation control can be obtained as

$$\bar{m}_{\text{true}} = \frac{z_d}{\alpha \gamma_z} A^{-1} \begin{bmatrix} \gamma_x & 0 & 0 \\ 0 & \gamma_y & 0 \\ 0 & 0 & 1 \end{bmatrix}^{-1} [p_d^T \ 1]^T. \quad (\text{A.8})$$

It can be seen from (A.8) that the robustness to uncertainties  $\gamma_x$  and  $\gamma_y$  can be improved by selecting  $\alpha$  arbitrarily high. This can also be verified from the expression in (39), where the rate of convergence of  $\alpha \hat{z}$  to  $z_d$  (i.e., the rate of decay of  $e_{v2}(t)$ ) can be improved by increasing  $\alpha$ .

Consider an example where  $\gamma_x$  and  $\gamma_y$  are varied from 0.5 to 1.5 while  $\gamma_z$  goes from 1 to 1.3. The results are shown in Fig. A.14; Fig. A.14A shows the image position of the fruit as a function of  $\gamma_x$  and  $\gamma_y$  for various  $\gamma_z$ ; Fig. A.14B shows the deviation  $e(t)$  of



$\bar{m}_{\text{true}}$  from the servoed position in the camera xy-plane. It can be seen from Fig. A.14A that the change in the fruit position in the CiH FOV is independent of the change in  $\gamma_z$ . From Fig. A.14B, it is clear that increasing the constant  $\alpha$  can lead to improved robustness to uncertainties.

In summary, the developed rotation controller is tolerant to uncertainties due to partial fruit detection, where the robustness can be improved by selecting a CiH with wide FOV. The translation controller is robust to depth uncertainties from partial fruit detection, and the robustness can be improved by increasing  $\alpha$ .

#### A.2. Overlapping and clustered fruit

The overlapping and clustered fruit pose an image processing challenge to detect individual fruits from the cluster. The presented visual servo controller relies on our previous work in Hannan et al. (2009) for fruit detection. The algorithm uses perimeter detection and shape analysis techniques to identify partially occluded or clustered (i.e., overlapping) fruit. In the presence of overlapping fruit, the depth estimator uses the major and minor axis of the fruit,  $d_{ix}$ ,  $d_{iy}$ , obtained from shape analysis techniques to estimate the fruit depth as listed in FootNote 1. Please note that the controller design remains unchanged in the presence of overlapping fruit.

#### A.3. Obstacles in the environment

Branches can affect operation of the robotic harvesting system in two ways. The presence of branches may result in partial or complete fruit occlusion. As shown in A.1, the developed visual servo controller is tolerant to partial fruit detection from partial occlusion. However, branches along the robot trajectory acting as obstacles may affect the performance of the visual servo controller and even damage the end-effector. In an effort to improve dexterity, we are investigating hybrid manipulators with continuum joint end-effectors for obstacle avoidance.

#### A.4. Fruit motion

Exogenous disturbances acting on a fruit, such as wind gust or robot-tree contact, may cause undesirable fruit motion that may affect the harvesting efficiency. The presented visual servo control relies on high-gain feedback for disturbance compensation. However, it is well-known that high-gain feedback controllers suffer in the presence of measurement noise. Advanced robust and adaptive control design methods should be adopted for compensating the unknown fruit motion, which remains an open problem. Our future research activities are focused on developing robust nonlinear control methods for disturbance compensation.

## References

- Brown, G.K., 2002. Mechanical harvesting systems for the Florida citrus juice industry. In: ASABE, St. Joseph, MI, pp. ASAE, Paper No. 021108.
- Buemi, F., Massa, M., Sandini, G., Costi, G., 1996. The agrobot project. *Adv. Space Res.* 18, 185–189.
- Ceres, R., Pons, F.L., Jimenez, A.R., Martin, F.M., Calderon, L., 1998. Design and implementation of an aided fruit-harvesting robot (Agribot). *Ind. Robot* 25, 337–346.
- d'Esnon, A.G., 1985. Robotic harvesting of apples. In: *Agri-Mation 1*, ASAE, Chicago, IL, pp. 25–28.
- d'Esnon, A.G., Rabatel, G., Pellenc, R., Journeau, A., Aldon, M.J., 1987. MAGALI: a self-propelled robot to pick apples. In: *Proceedings of American Society of Agricultural Engineers*, Baltimore, Maryland.
- Hannan, M.W., Burks, T.F., 2004. Current developments in automated citrus harvesting. In: *ASABE Annual International Meeting*.
- Hannan, M.W., Burks, T.F., Bulanog, D.M., 2009. A machine vision algorithm combining adaptive segmentation and shape analysis for orange fruit detection. *Agricult. Eng. Int.: CIGR Ejournal* XI, 1–17.
- Harrell, R., Adsit, P., Munilla, R., Slaughter, D., 1990a. Robotic picking of citrus. *Robotica* 8, 269–278.
- Harrell, R., Adsit, P., Pool, T., Hoffman, R., et al., 1990b. The Florida robotic grove-lab. *Trans. ASAE* 33, 391–399.
- Harrell, R., Slaughter, D., Adsit, P., 1989. A fruit-tracking system for robotic harvesting. *Mach. Vis. Appl.* 2, 69–80.
- Juste, F., Sevilla, F., 1992. Citrus: an European project to study the robotic harvesting of oranges. *Rapport. Institut for Jordbrugsvidenskab*.
- Kondo, N., Nishitsuji, Y., Ling, P., Ting, K., 1996. Visual feedback guided robotic cherry tomato harvesting. *Trans. ASAE* 39, 2331–2338.
- Levi, P., Falla, A., Pappalardo, R., 1988. Image controlled robotics applied to citrus fruit harvesting. In: *7th International Conference on Robot Vision and Sensory Controls*. IFS Publications, Zurich, Switzerland, pp. 2–4.
- Li, P., Lee, S.h., Hsu, H.Y., 2011. Review on fruit harvesting method for potential use of automatic fruit harvesting systems. *Proc. Eng.* 23, 351–366.
- Malis, E., Chaumette, F., 2002. Theoretical improvements in the stability analysis of a new class of model-free visual servoing methods. *IEEE Trans. Robotics Automat.* 18, 176–186.
- Muraro, R., Spreen, T., Roka, F., 2000. Focus on brazil: the impact of the 1999 Brazilian devaluation on the delivered-in costs of oranges produced in são paulo. *Citrus Industry*, 20–22.
- Muscato, G., Prestifilippo, M., Abbate, N., Rizzuto, I., 2005. A prototype of an orange picking robot: past history, the new robot and experimental results. *Indust. Robot: An Int. J.* 32, 128–138.
- Rabatel, G., Bourelly, A., Sevilla, F., Juste, F., 1995. Robotic harvesting of citrus: state-of-art and development of the French Spanish EUREKA project. *Proceedings of International Conference on Harvest and Post Harvest Technologies for Fresh Fruits and Vegetables*, 232–239.
- Recce, M., Taylor, J., Plebe, A., Tropiano, G., 1996. Vision and neural control for an orange harvesting robot. In: *Proceedings of the International Workshop on Neural Networks for Identification, Control, Robotics, and Signal/Image Processing*, 1996, pp. 467–475.
- Sarig, Y., 1993. Robotics of fruit harvesting: a state-of-the-art review. *J. Agricult. Eng.* 54, 265–280.
- Spreen, T., Muraro, R., 2000. The World Market for Citrus Products and Risk Management for Florida Citrus Growers, Economic Information Report. Technical Report. Food and Resource Economics Department, University of Florida, Gainesville, FL.
- Tillett, N., 1993. Robotic manipulators in horticulture: a review. *J. Agricult. Eng. Res.* 55, 89–105.
- Van Henten, E., Hemming, J., Van Tuijl, B., Kornet, J., Bontsema, J., 2003. Collision-free motion planning for a cucumber picking robot. *Biosyst. Eng.* 86, 135–144.
- Van Henten, E., Hemming, J., Van Tuijl, B., Kornet, J., Meuleman, J., Bontsema, J., Van Os, E., 2002. An autonomous robot for harvesting cucumbers in greenhouses. *Autonom. Robots* 13, 241–258.
- Zhang, Z., 2000. A flexible new technique for camera calibration. *IEEE Trans. Pattern Anal. Mach. Intell.* 22, 1330–1334.